Supporting Information

Subcomponent Self-Assembly of Circular Helical $Dy_6(L)_6$ and Bipyramid $Dy_{12}(L)_8$ Architectures Directed via Second-Order Template Effects

Xiao-Lei Li,[a,b] Lang Zhao,[a] Jianfeng Wu,[a] Wei Shi,[b]* Niklas Struch,[c]
Arne Lützen,[c]* Annie K. Powell,[d]* Peng Cheng[b] and Jinkui Tang[a,e]*

[a]State Key Laboratory of Rare Earth Resource Utilization, Changchun Institute of Applied Chemistry, Chinese Academy of Sciences, Changchun 130022, P. R. China
[b]Key Laboratory of Advanced Energy Materials Chemistry (Ministry of Education), College of Chemistry, Nankai University, Tianjin 300071, P. R. China
[c]Kekulé Institute of Organic Chemistry and Biochemistry, Rheinische-Friedrich-Wilhelms-University of Bonn, Gerhard- Domagk-Str. 1, D-53121 Bonn, Germany
[d]Institute of Inorganic Chemistry, Karlsruhe Institute of Technology, Engesserstrasse 15, 76131 Karlsruhe, Germany and Institute of Nanotechnology, Karlsruhe Institute of Technology, Hermann-von-Helmholtz-Platz 1, Eggensteinn- Leopoldshafen, 76344 Karlsruhe, Germany
[e]University of Science and Technology of China, Hefei 230026, P. R. China

Table of Contents

Experimental Procedures

Synthesis of 4, 6-dihydroxypyrimidine

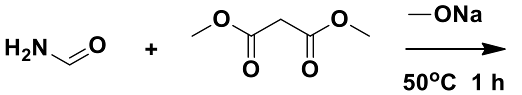

To a stirred solution of sodium methoxide (140 g, 0.7 mol of a 27%-solution in methanol) was added formamide (27.0 g, 0.6 mol) under nitrogen atmosphere over about 5 minutes. The resulting reaction mixture was heated to 50 °C, and then dimethyl malonate (26.4 g, 0.2 mol) was added dropwise over 1 h. The resulting white suspension was held at 50 °C for a further hour and then allowed to cooled to ambient temperature. Water (100 mL) was added to dissolve all the solid and the resulting straw-colored solution was stirred for about 15 min and then the methanol was removed under vacuum (final pot at 50 °C under 100 mmHg vacuum). Water (40 mL) was added followed by 36% sulfuric acid (90 g) to adjust a final pH of 2.2. Once the acid had been added the temperature was kept at about 35 °C. The yellow suspension was stirred for 1 h, filtered and washed with water (2 × 25 g). The water-wet paste was dried overnight under vacuum at 50 °C to provide 4, 6-dihydroxypyrimidine (16.2 g, 70% yield).

Synthesis of the 4, 6-dichloropyrimidine

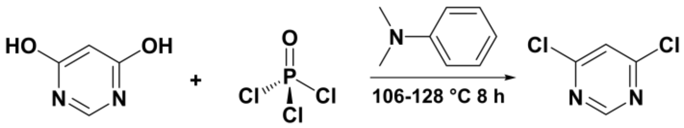

46 g of phosphorus oxychloride and 6.2 g of *N*,*N*-dimethylaniline were mixed. 11.6 g of 4, 6-dihydroxypyrimidine (98% purity) were added into the mixture with a screw at 100 °C over a period of 5 hours. Thereafter, the reaction mixture was subsequently stirred at 106 °C to 128 °C for 8 hours. It was diluted with 30 g of chlorobenzene and the resulting mixture poured onto 120 g of ice. The organic phase was separated off, washed twice with 10 mL of water and then subjected to fractional distillation. 8.57 g of 4,6- dichloropyrimidine (58% yield) were obtained.

Synthesis of 4, 6-dihydrazinopyrimidine

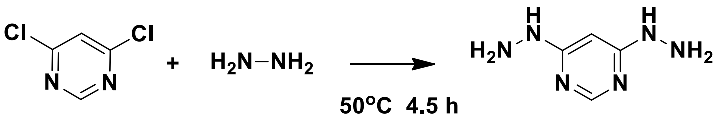

10 mL of methanol were added to 13 mL of hydrazine monohydrate and the resulting mixture was cooled to 10 °C (internal temperature). 5.0 g (33.6 mmol) of 4,6-dichloropyrimidine were added gradually to this mixture is gradually added to keep the internal temperature at 20 °C or less. After complete addition the reaction mixture was stirred for 4 h and then heated for 30 min to 50 °C. The precipitated crystals were collected by filtration, washed with isopropanol, and dried to obtain 4.31 g (92% yield) of the intermediate 4,6-dihydrazinopyrimidine as a white powder.

IR and MS characterization of lanthanide complexes

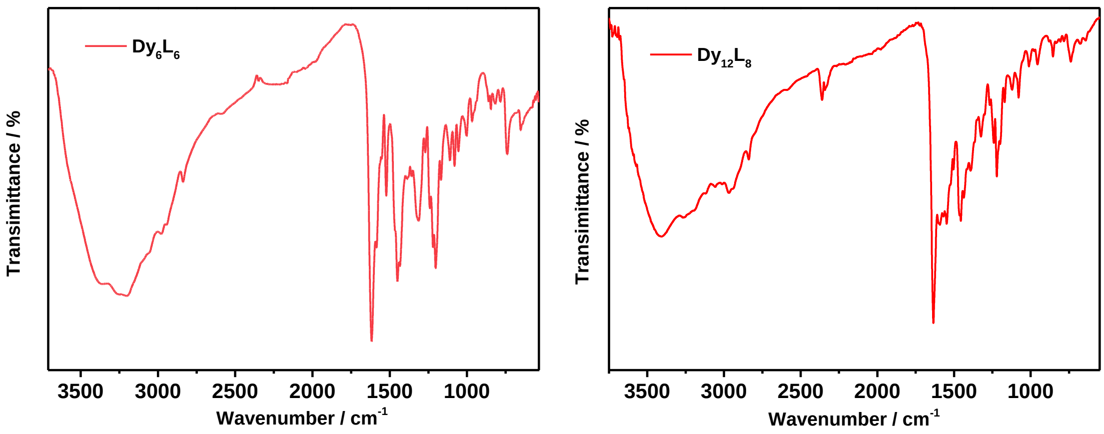

Figure S1. IR spectra of complexes **$Dy_6(L)_6$** (left) and **$Dy_{12}(L)_8$** (right).

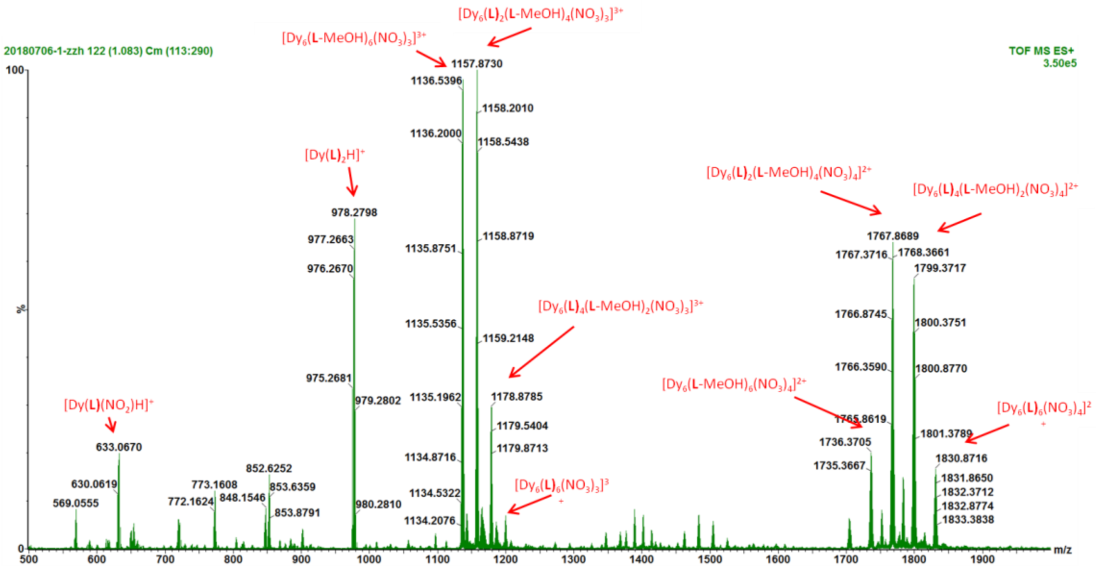

Figure S2. ESI mass spectrum of **$Dy_6(L)_6$**.

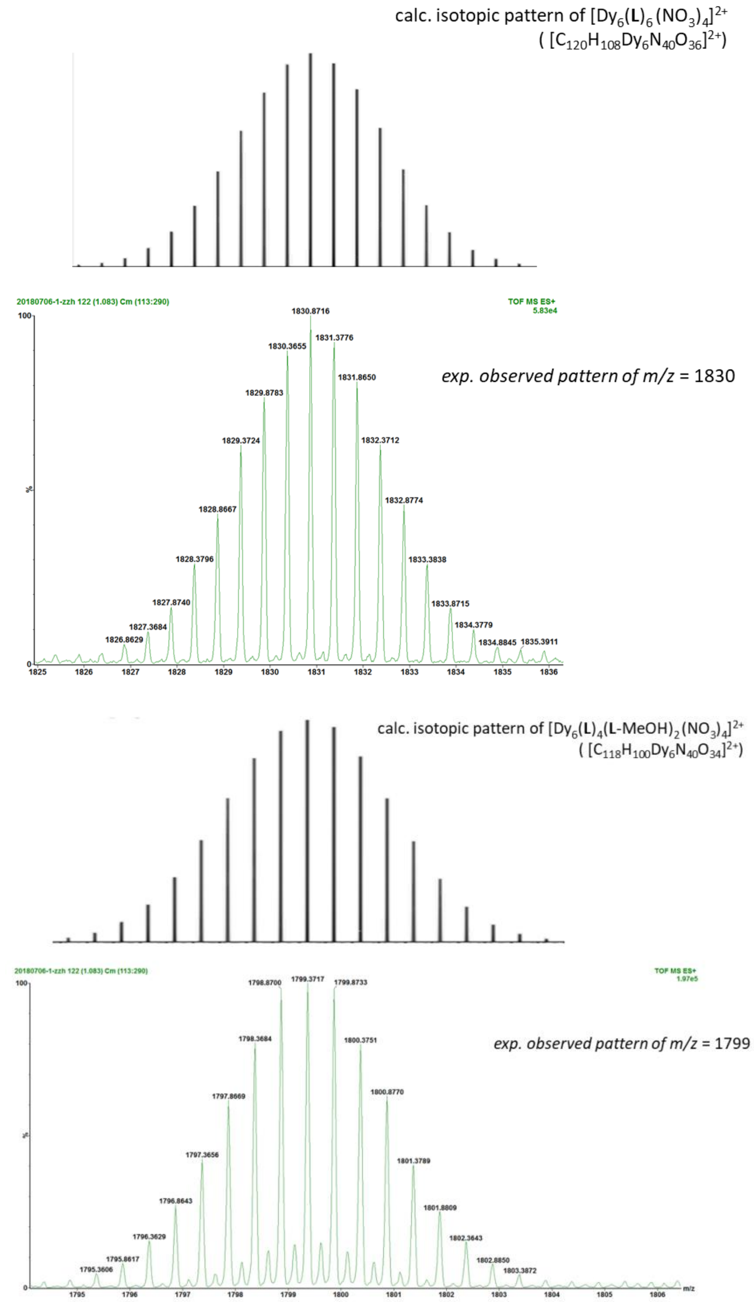

Figure S3. ESI mass spectrum of **$Dy_6(L)_6$** – comparison of experimentally observed and calculated isotopic patterns of signals at *m/z* 1799 (bottom) and *m/z* 1830 (top).

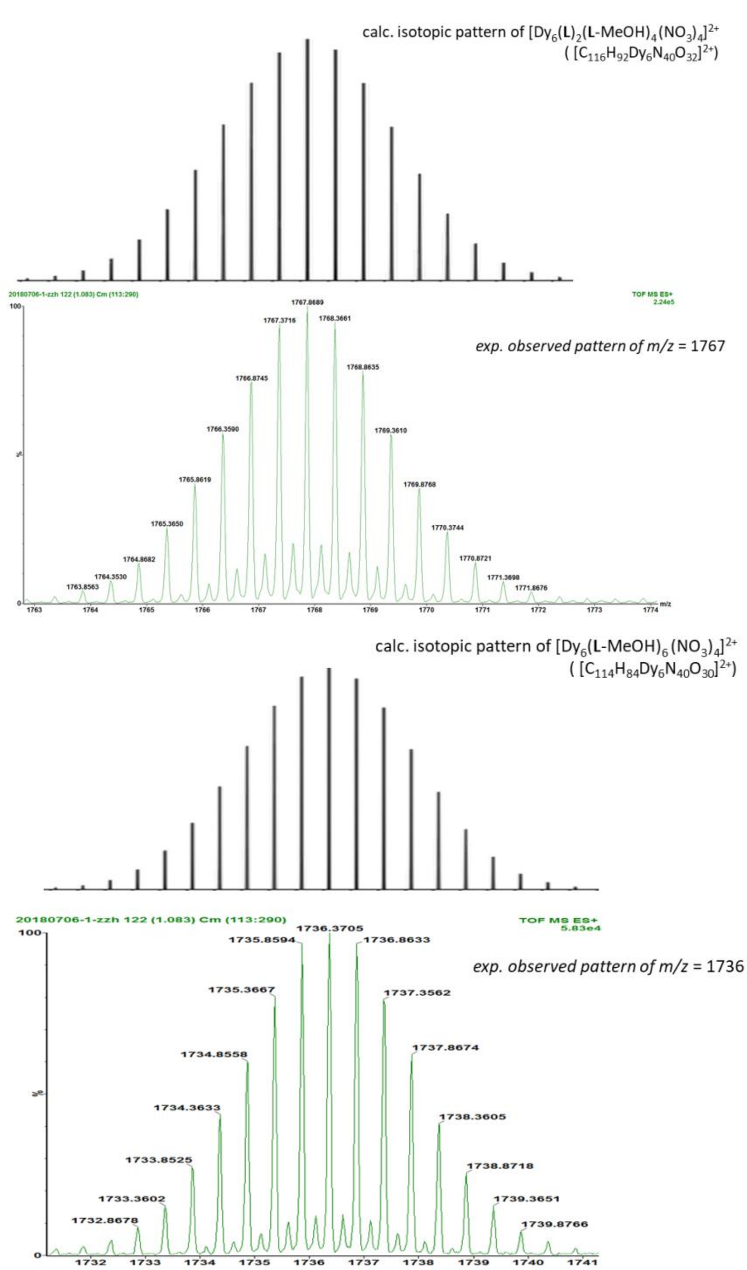

Figure S4. ESI mass spectrum of **$Dy_6(L)_6$** – comparison of experimentally observed and calculated isotopic patterns of signals at *m/z* 1736 (bottom) and *m/z* 1767 (top).

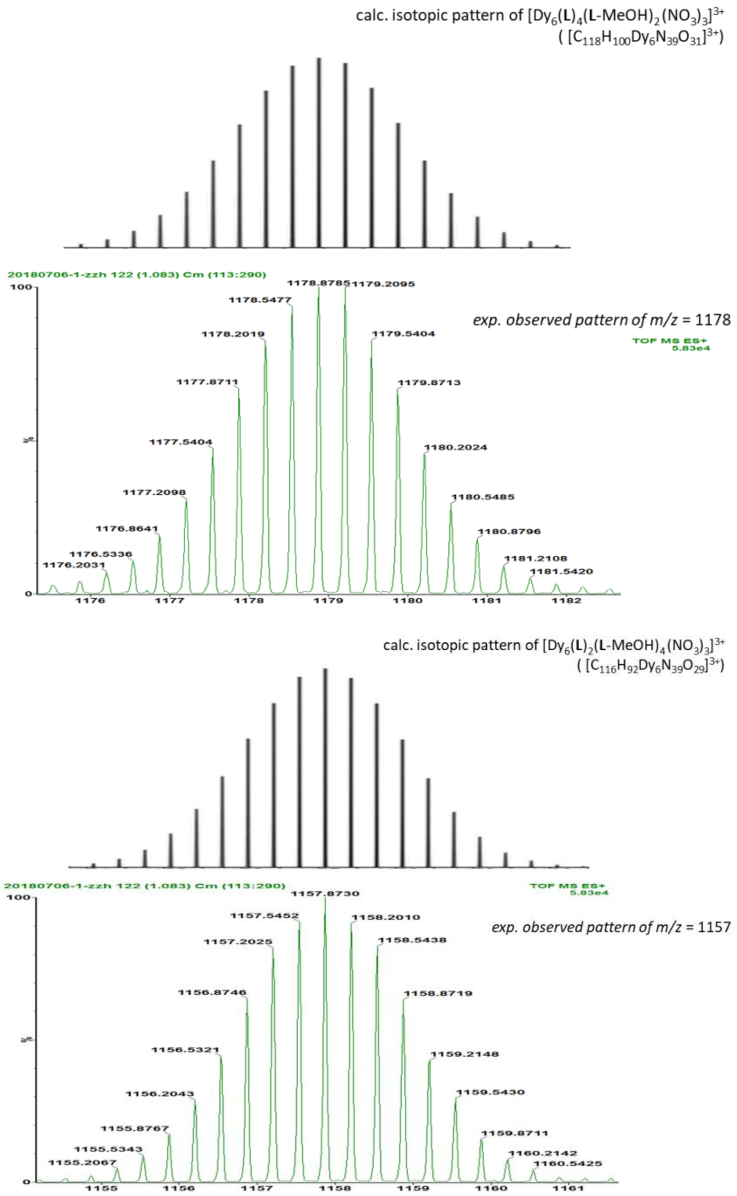

Figure S5. ESI mass spectrum of $\mathbf{Dy_6(L)_6}$ – comparison of experimentally observed and calculated isotopic patterns of signals at *m/z* 1157 (bottom) and *m/z* 1178 (top).

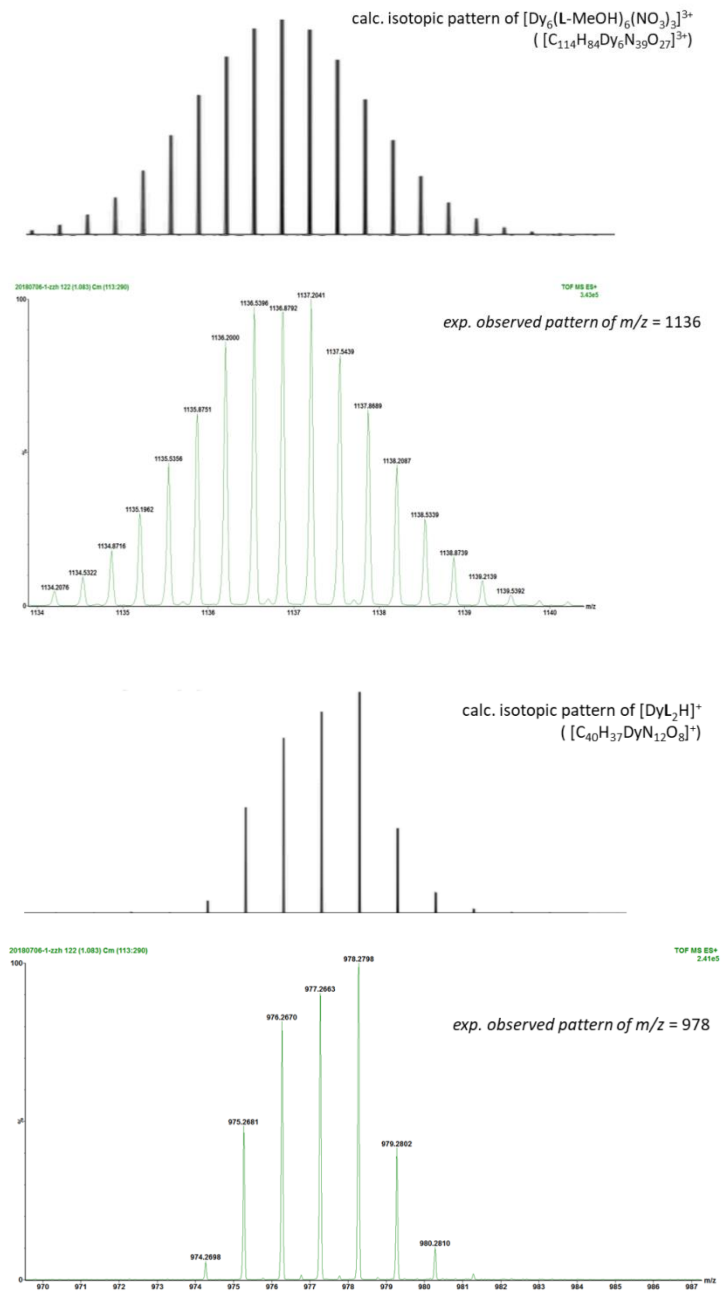

Figure S6. ESI mass spectrum of $\mathbf{Dy_6(L)_6}$ – comparison of experimentally observed and calculated isotopic patterns of signals at *m/z* 978 (bottom) and *m/z* 1136 (top).

X-ray Crystal Structure Determinations

Table S1. Crystal data and structure refinement for **$Dy_6(L)_6$** and **$Dy_{12}(L)_8$**

Compound	$Dy_6(L)_6$	$Dy_{12}(L)_8$
Empirical formula	$C_{143}Dy_6N_{43}O_{75}H_{198}$	$C_{224}H_{222}Dy_{12}N_{50}Na_4O_{94}$
Formula weight	4694.43	7160.46
Temperature/K	100	100
Crystal system	monoclinic	tetragonal
Space group	$P2_1/n$	$I4_1/acd$
a/Å	25.480(3)	32.0539(6)
b/Å	23.024(3)	32.0539(6)
c/Å	39.629(4)	56.6487(17)
α/°	90	90
β/°	90.666(2)	90
γ/°	90	90
Volume/Å^3	23247(5)	58204(3)
Z	4	8
ρ_{calc} g/cm^3	1.341	1.634
F(000)	9412.0	28032.0
Independent reflections	45888 [R_{int} = 0.0805, R_{sigma} = 0.0887]	17461 [R_{int} = 0.0831, R_{sigma} = 0.0900]
Goodness-of-fit on F^2	1.019	1.023
Final R indexes [I > =2σ (I)]	*R_1 = 0.0578, wR_2 = 0.1417	*R_1 = 0.0807, wR_2 = 0.2040
Final R indexes [all data]	*R_1 = 0.1076, wR_2 = 0.1678	*R_1 = 0.1725, wR_2 = 0.2833

*$R_1 = \Sigma||Fo| - |Fc||/\Sigma|Fo|$ for $Fo > 2\sigma(Fo)$; $wR_2 = (\Sigma w(Fo^2 - Fc^2)^2/\Sigma(wFc^2)^2)^{1/2}$ all reflections, $w = 1/[\sigma^2(Fo^2)+(0.1824P)^2 + 60.585P]$ where $P = (Fo^2+2Fc^2)/3$

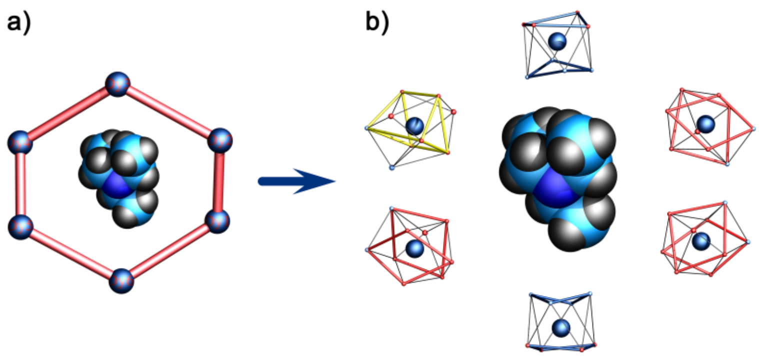

Figure S7. a) Frame-and-sphere representations of the six Dy^{III} centers roughly arranged into a hexagon where the NEt_3 molecule occupying the central cavity is shown as a space-filling model. b) Coordination polyhedral observed in **$Dy_6(L)_6$** showing spherical capped square antiprism geometries for Dy1/Dy2/Dy5; tricapped trigonal prism geometry for Dy4 and square antiprismatic geometries for Dy3/Dy6.

Table S2. Corresponding distances and angles of Dy_6 hexagon in Figure S7a.

Distances		Angles	
Dy1–Dy2	6.885 Å	Dy1–Dy2–Dy3	111.78°
Dy4–Dy5	6.882 Å	Dy2–Dy3–Dy4	120.50°
Dy2–Dy3	9.151 Å	Dy3–Dy4–Dy5	113.91°
Dy3–Dy4	9.145 Å	Dy4–Dy5–Dy6	116.02°
Dy5–Dy6	8.931 Å	Dy5–Dy6–Dy1	119.81°
Dy6–Dy1	8.920 Å	Dy6–Dy1–Dy2	116.67°

Table S3. Corresponding distances and angles of Dy_6 hexagon in Figure S7a.

Dy^{III}	CSAPR-9 (C_{4v})	JTCTPR-9 (D_{3h})	TCTPR-9 (D_{3h})	JCSAPR-9 (C_{4v})	CCU-9 (C_{4v})
Dy^{III}(1)	**1.632**	1.663	1.942	2.382	8.731
Dy^{III}(2)	**1.685**	1.812	1.947	2.399	7.804
Dy^{III}(4)	1.722	**1.685**	1.974	2.452	8.325
Dy^{III}(5)	**1.708**	1.716	1.843	2.486	8.337
	BTPR-8 (C_{2v})	**TDD-8 (D_{2d})**	**SAPR-8 (D_{4d})**	**JBTPR-8 (C_{2v})**	**JSD-8 (D_{2d})**
Dy^{III}(3)	**1.249**	1.407	1.524	1.613	3.786
Dy^{III}(6)	**0.894**	1.839	1.766	1.327	3.958

CSAPR-9 = Spherical capped square antiprism; JTCTPR-9 = Tricapped trigonal prism J51; TCTPR-9 = Spherical tricapped trigonal prism; JCSAPR-9 = Capped square antiprism J10; CCU-9 = Spherical-relaxed capped cube. TDD-8 = Triangular dodecahedron; SAPR-8 = Square antiprism; BTPR-8 = Biaugmented trigonal prism; JBTPR-8 = Biaugmented trigonal prism J50; JSD-8 = Snub diphenoid J84.

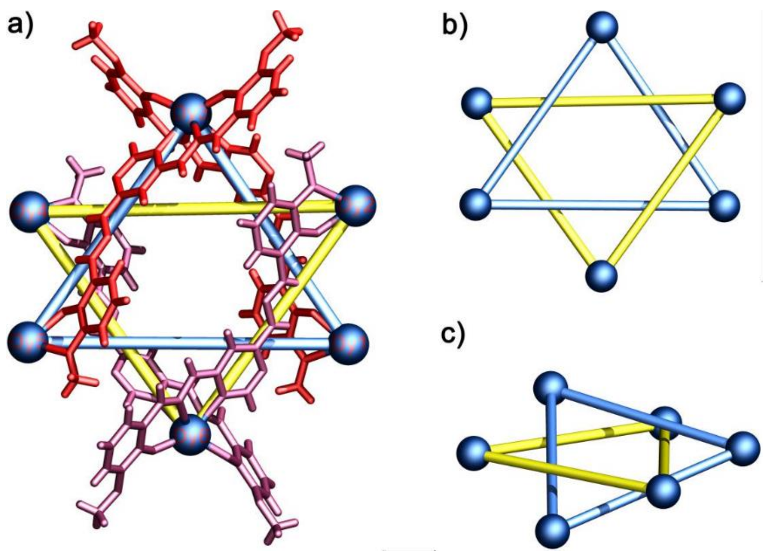

Figure S8. a) Frame-and-sphere representations of quadruple-stranded helical $\mathbf{Dy_6(L^C)_4}$ which consists of two interwoven triangles $\mathbf{Dy_3(L^C)_2}$, blue and yellow triangles represent triangle Dy1, Dy3, Dy5 and Dy2, Dy4, Dy6, respectively. b) Two interwoven triangles colored by blue and yellow with ligands omitted for clarity. c) Two interwoven triangles shown along the planar direction.

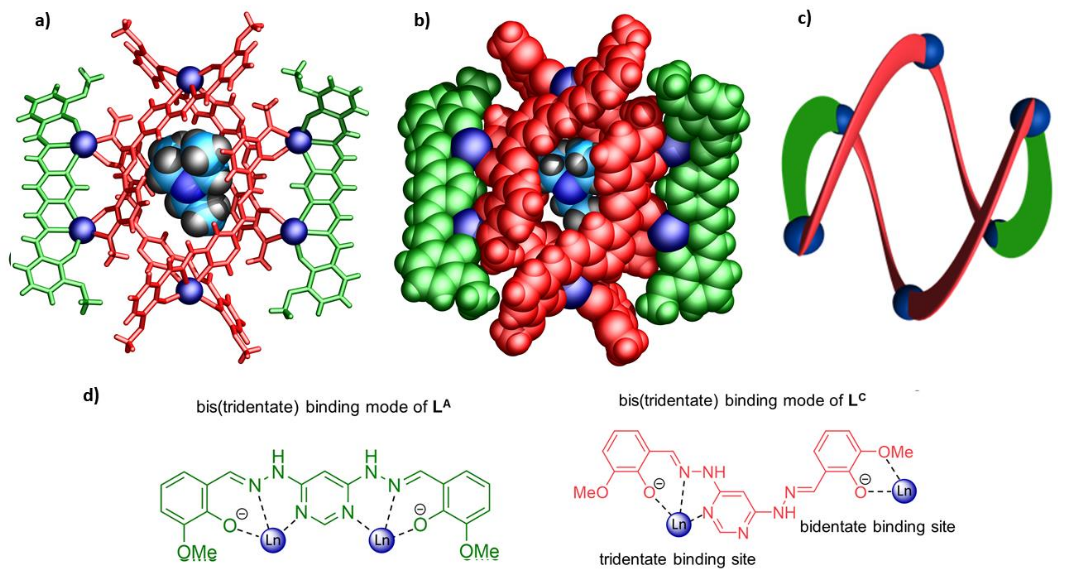

Figure S9. a) Frame-and-sphere representation of the supramolecular aggregate **$Dy_6(L)_6$** where the NEt_3 molecule occupying the central cavity is shown as a space-filling model and ligands **L^A** and **L^C** have been colored in green and red as in Scheme 1, respectively; b) The space-filling model of same representation (coordinating nitrate ions and water and methanol molecules are omitted for clarity); c) Schematic representation of the circular helicate. d) Representation of the different binding modes of ligands **L^A** and **L^C** in this assembly.

Table S4. Corresponding distances and angles of two interwoven trinuclear Dy_3 triangles in Fig. S3.

	Distances		**Angles**	
Blue triangle	Dy1···Dy3	13.338 Å	Dy1···Dy3···Dy5	70.291°
	Dy3···Dy5	13.491 Å	Dy3···Dy5···Dy1	54.390°
	Dy1···Dy5	15.444 Å	Dy5···Dy1···Dy3	55.319°
Yellow triangle	Dy2···Dy4	15.884 Å	Dy2···Dy6···Dy4	72.225°
	Dy2···Dy6	13.494 Å	Dy6···Dy4···Dy2	53.999°
	Dy4···Dy6	13.456 Å	Dy4···Dy2···Dy6	53.776°
			Dihedral Angle	18.531°

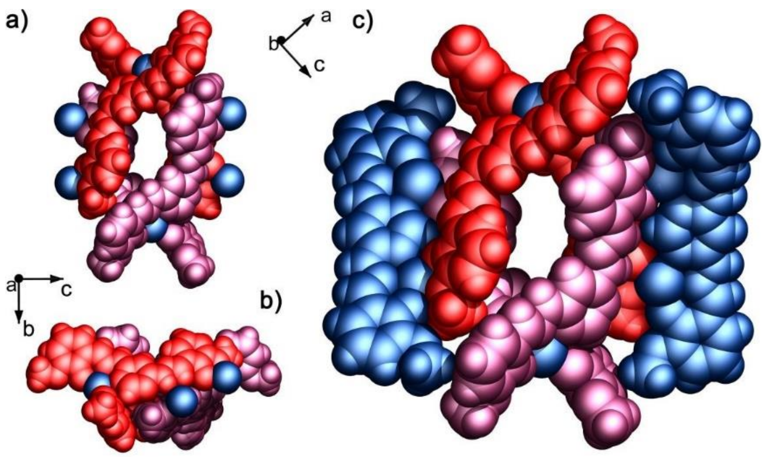

Figure S10. a, b) Space-filling representation of the crystal structure of double-stranded helicate intermediate **$Dy_6(L^C)_4$** along *a* and *b* axis. c) Space-filling representation of **$Dy_6(L_6)$**, highlighting the helical and linear arrangement of the ligands around the Dy^{III} ions. For clarity, each type of ligand is represented in a different color, NEt_3 template in the central cavity, coordinated methanol, water molecules and NO_3^- ions are omitted.

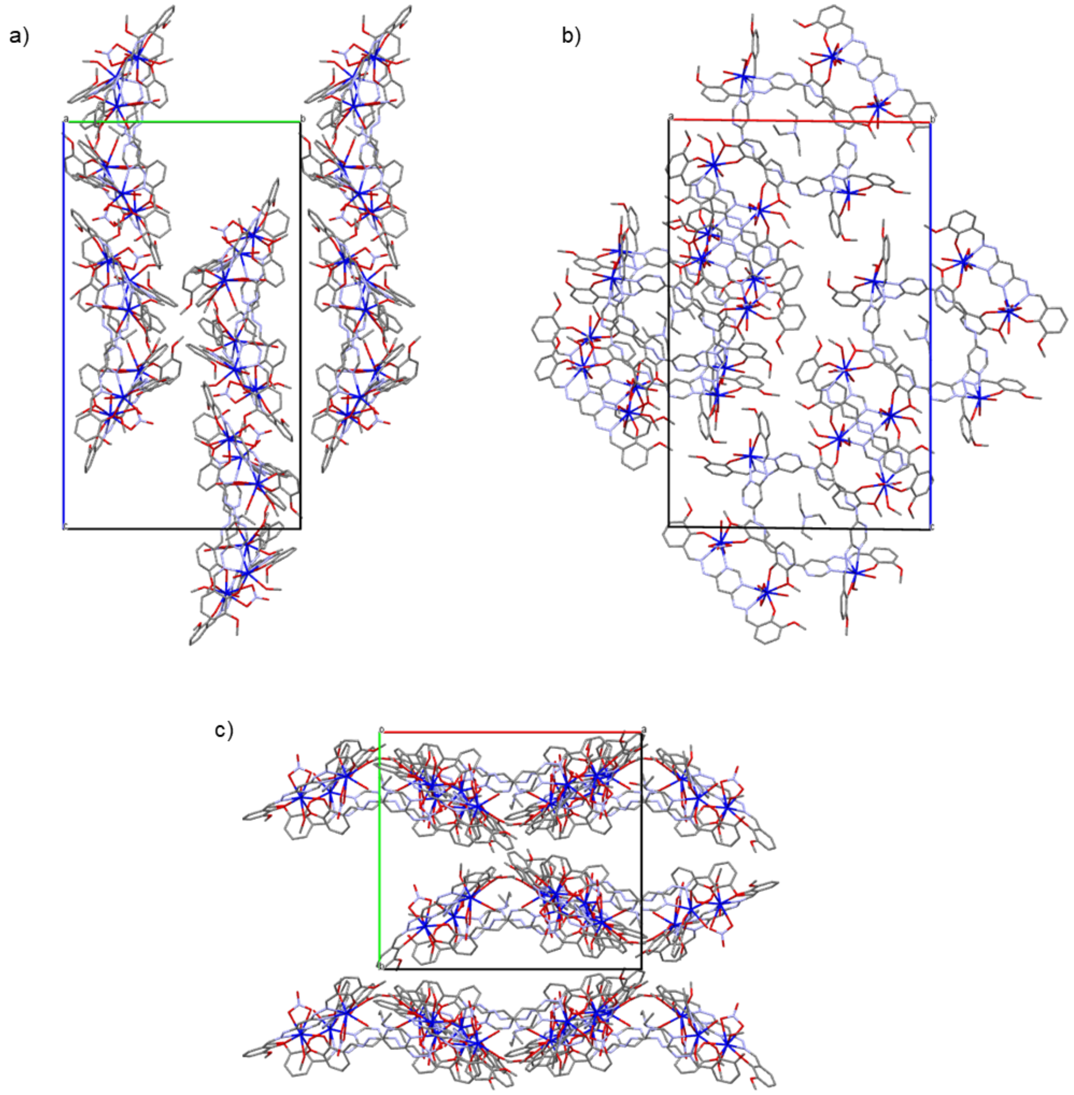

Figure S11. Crystallographic packing of discrete $\mathbf{Dy_6(L)_6}$ aggregates: a) view along the crystallographic a axis, b) view along the crystallographic b axis, and c) view along the crystallographic c axis (hydrogen atoms as well as non-coordinating solvent molecules and counterions are omitted, color code: C gray, N light blue, O red, Dy dark blue).

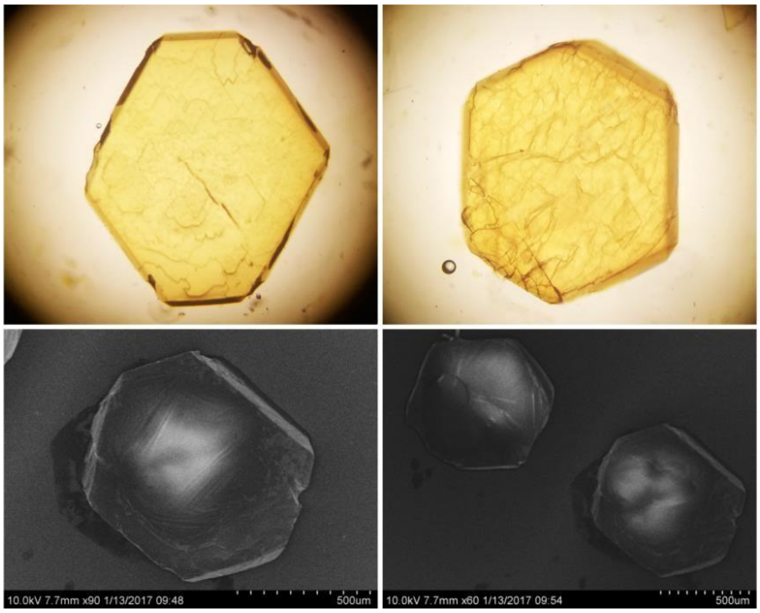

Figure S12. Optical (top) and SEM (bottom) images of the crystals of complex $\mathbf{Dy_6(L)_6}$.

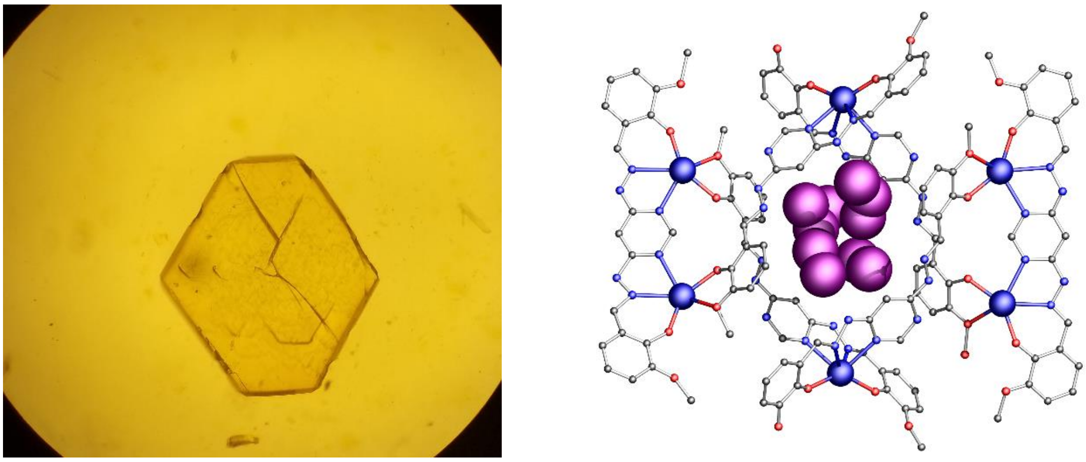

Figure S13. Optical microscopy image of crystals of complex $\mathbf{Dy_6(L)_6}$ (left) obtained using amino-2-propanol instead of NEt_3 as a base and template in the subcomponent self-assembly approach. Single crystal XRD analysis showed the same circular helicate architecture (right) with the following cell parameters: a = 25.480(3) Å, b = 23.024(3) Å, c = 39.629(4) Å, α = 90º, β = 95.86º, γ = 90º and V = 20021 Å^3. Unfortunately, however, the poor quality of the data, did not allow to solve the full structure in a satisfying manner.

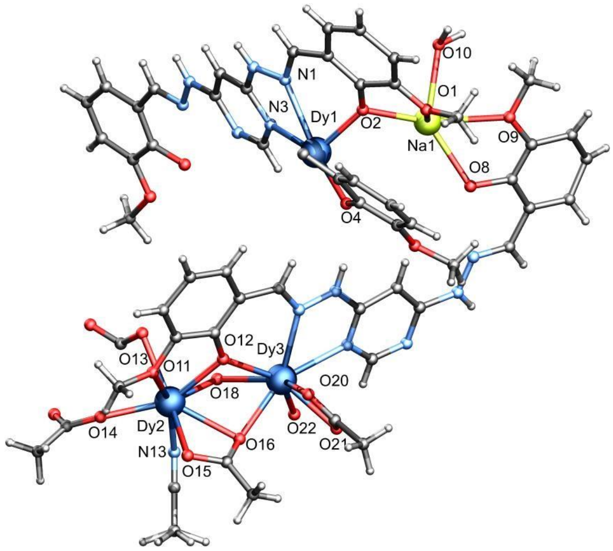

Figure S14. Asymmetric unit of the crystal structure of $\mathbf{Dy_{12}(L)_8}$ with atom numbering scheme.

Table S5. Dy^{III} geometry analysis of $\mathbf{Dy_{12}(L)_8}$ by SHAPE 2.1 software.[1]

$\mathbf{Dy^{III}}$	**CSAPR-9 (*C*$_{4v}$)**	**JTCTPR-9 (*D*$_{3h}$)**	**TCTPR-9 (*D*$_{3h}$)**	**JCSAPR-9 (*C*$_{4v}$)**	**CCU-9 (*C*$_{4v}$)**
$\mathbf{Dy^{III}(2)}$	**1.947**	2.816	3.180	2.543	9.446
$\mathbf{Dy^{III}(3)}$	**1.549**	3.041	2.000	2.201	8.706
	BTPR-8 (*C*$_{2v}$)	**TDD-8 (*D*$_{2d}$)**	**SAPR-8 (*D*$_{4d}$)**	**JBTPR-8 (*C*$_{2v}$)**	**JSD-8 (*D*$_{2d}$)**
$\mathbf{Dy^{III}(1)}$	2.044	**1.519**	2.913	2.600	4.359

CSAPR-9 = Spherical capped square antiprism; JTCTPR-9 = Tricapped trigonal prism J51; TCTPR-9 = Spherical tricapped trigonal prism; JCSAPR-9 = Capped square antiprism J10; CCU-9 = Spherical-relaxed capped cube. TDD-8 = Triangular dodecahedron; SAPR-8 = Square antiprism; BTPR-8 = Biaugmented trigonalprism; JBTPR-8 = Biaugmented trigonal prism J50; JSD-8 = Snub diphenoid J84.

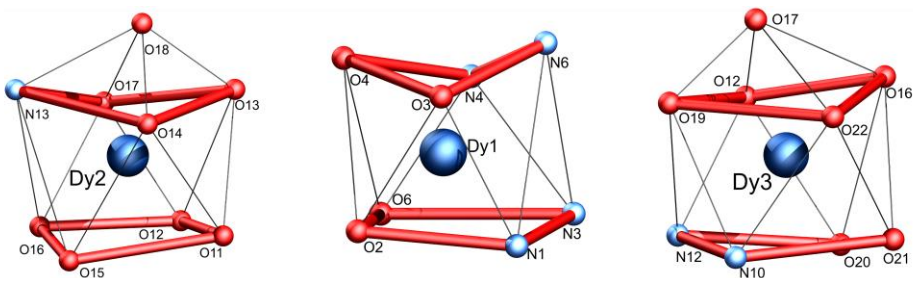

Figure S15. Coordination polyhedral observed in $\mathbf{Dy_{12}(L)_8}$ showing spherical capped square antiprism geometries for Dy2/Dy3; Triangular dodecahedron for Dy1.

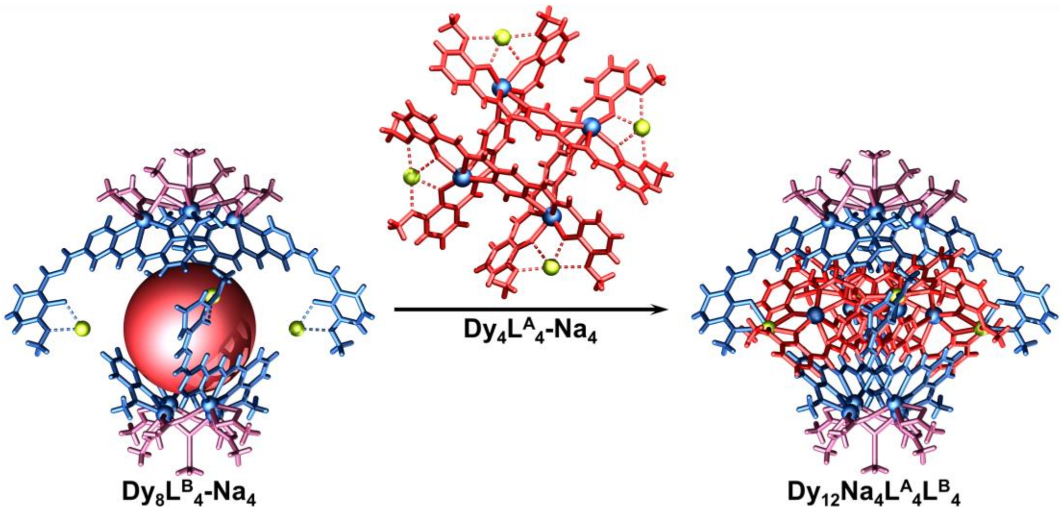

Figure S16. Frame-and-sphere representations of the $\mathbf{Dy_{12}(L)_8}$ and its two components $\mathbf{Dy_8(L^B)_4\text{-}Na_4}$ and $\mathbf{Dy_{4(}L^A)_4\text{-}Na_4}$. For clarity, each type of ligand is represented in different color, with Dy^{III} and Na^+ ions represented by yellow and blue spheres, coordinated o-vanillin, water molecules, CO_3^{2-} and solvent molecules are not shown.

The core structure of $\mathbf{Dy_{12}L_8}$ is shown in Figure S14, this core structure can be reduced into a smaller truncated octahedron (Octa-2) encapsulated in the central cavity of a bigger truncated octahedron (Octa-1) with two shared top and bottom Dy_4 grids. The combined truncated octahedron is constructed by three layers of grids (two Dy_4 grids and one Na_4 grid) of different size (Figure S15).

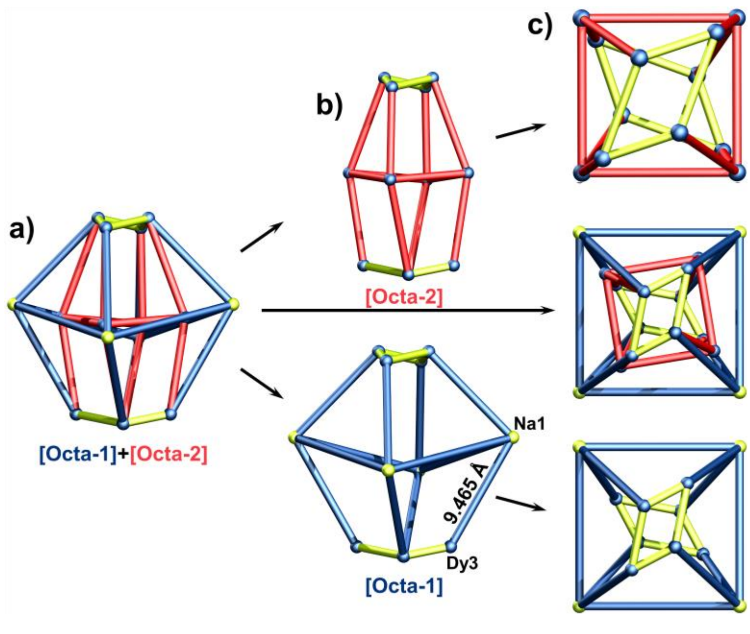

Figure S17. a) Frame-and-sphere representations of the $\mathbf{Dy_{12}Na_4}$ core highlighting two distorted octahedrons with two truncated angles in top and bottom sides. b) The $\mathbf{Dy_{12}Na_4}$ core is split into two distorted octahedron parts. c) Top views for the Figure a) and b). Color scheme: Dy, blue; Na, yellow.

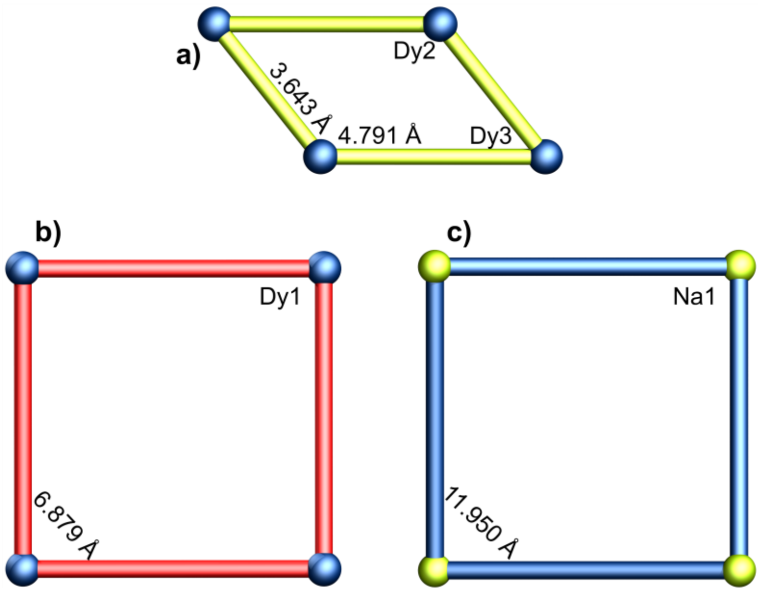

Figure S18. Frame-and-sphere representations of the three layers of grids with different size in truncated octahedrons shown in Figure S8. a) Top and bottom Dy_4 grids with smallest size. b) and c) Bigger Dy_4 grid and the Na_4 grid with the biggest size in the middle of the distorted octahedron. Color scheme: Dy, blue; Na, yellow.

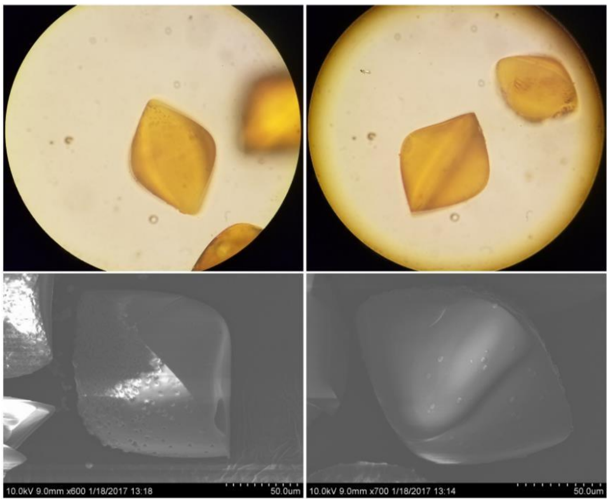

Figure S19. Optical (top) and SEM (bottom) images of the crystals of complex $\mathbf{Dy_{12}(L)_8}$.

a)

b)

c)

d)

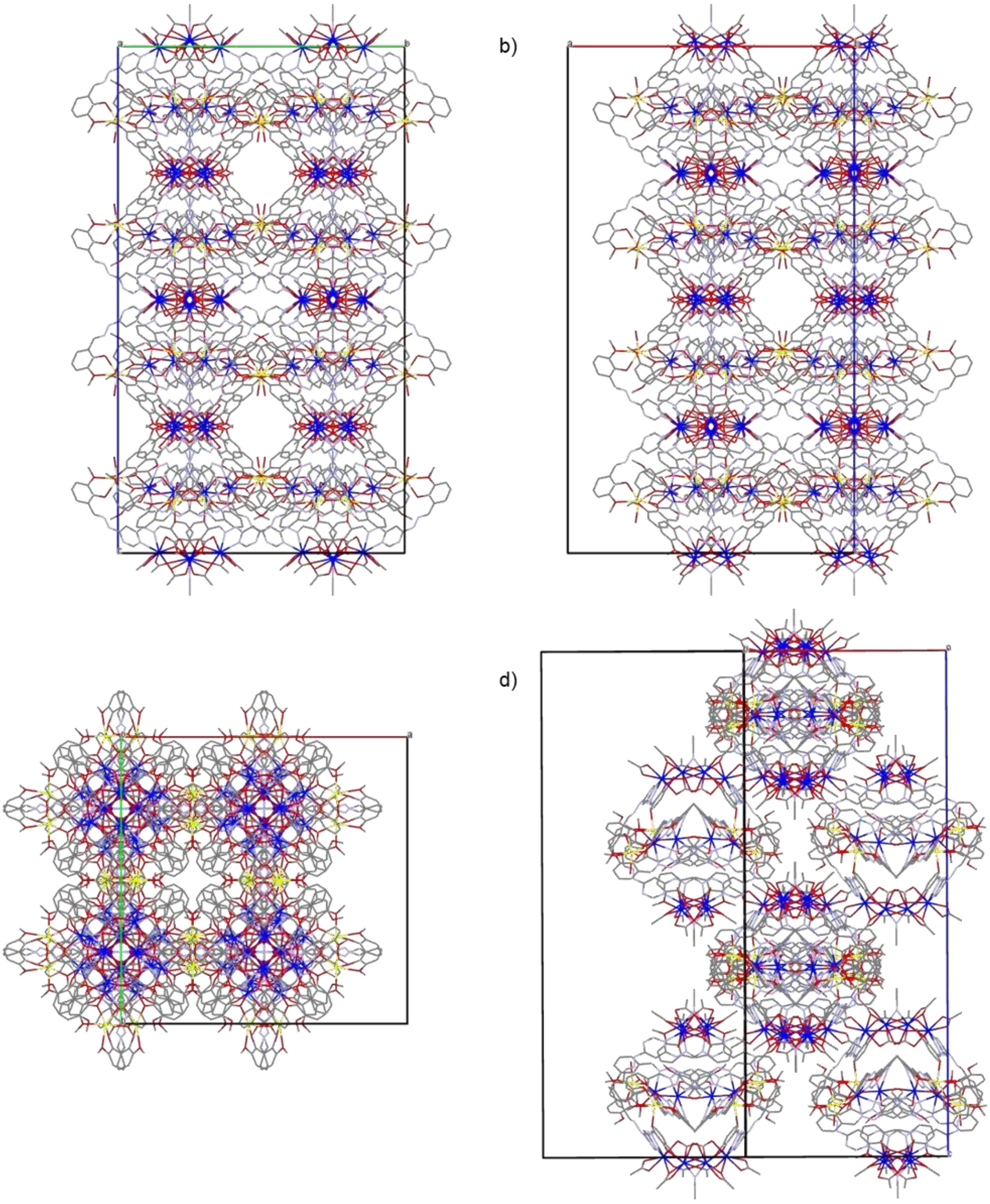

Figure S20. Crystallographic packing of discrete **$Dy_{12}(L)_8$** aggregates: a) view along the crystallographic a axis, b) view along the crystallographic b axis, c) view along the crystallographic c, and d) view along the bisecting angle between crystallographic axes a and b (hydrogen atoms as well as non-coordinating solvent molecules and counterions are omitted, color code: C gray, N light blue, O red, Dy dark blue, Na yellow-green).

Magnetic Measurements

Table S6. Reported multinuclear lanthanide SMMs with $\boldsymbol{U_{eff}}$ larger than 200 K in the literature.

Complexes	Abbrev.	U_{eff} (K)	Ref.[a]
$[Dy_6(L^A)_2(L^B)_4(CH_3OH)_7(H_2O)_5(NO_3)_4]\cdot NEt_3\cdot 10CH_3OH\cdot 11H_2O\cdot 2NO_3$	**Dy_6L_6**	**254/435**	**this work**
$[Dy_6(\mu_3\text{-}OH)_4L_4L'_2\text{-}(H_2O)_9Cl]Cl_5\cdot 15H_2O$	Dy_6	200	30a
$[Ln_5O(OiPr)_{13}]$ Ln = Dy, Ho	Dy_5	528/400	30b,c
$[Dy_4K_2O(OtBu)_{12}]\cdot C_6H_{14}$	Dy_4K_2	316/692	30i
$[Dy_4(OH)_2(bpt)_4(NO_3)_4(OAc)_2]$	Dy_4	205	30d
$[(\eta_5\text{-}Cp'_2Dy)\{\mu\text{-}Sb(H)Mes\}]_3$	1-Dy (Dy_3)	496	30f
$[(\eta_5\text{-}Cp'_2Dy)_3\{\mu\text{-}(SbMes)_3Sb]$	2-Dy (Dy_3)	388	30f
$[(\eta_5\text{-}Cp'_2Dy)\{\mu\text{-}As(H)Mes\}]_3$	4-Dy (Dy_3)	368	30e
$[(\eta_5\text{-}Cp'_2Dy)\{\mu\text{-}SeMes\}]_3$	6-Dy (Dy_3)	362	30e
$[Dy(\mu\text{-}OH)(DBP)_2(THF)]_2$	Dy_2	721	30g
$\{[(Me_3Si)_2N]_2(THF)Ln\}_2(\mu\text{-}\eta^2\text{:}\eta^2\text{-}N_2)$	Tb_2	326	30h
$(Cp^{iPr5})_2Dy_2I_3$	1-Dy	2346	30j
$(Cp^{iPr5})_2Tb_2I_3$	1-Tb	1990	30j

[a] reference numbers refer to the numbers listed in the main text (and below).

a) I. J. Hewitt, J. Tang, N. T. Madhu, C. E. Anson, Y. Lan, J. Luzon, M. Etienne, R. Sessoli and A. K. Powell, *Angew. Chem. Int. Ed.*, 2010, **49,** 6352;
b) R. J. Blagg, C. A. Muryn, E. J. L. McInnes, F. Tuna and R. E. P. Winpenny, *Angew. Chem. Int. Ed.*, 2011, **50,** 6530;
c) R. J. Blagg, F. Tuna, E. J. L. McInnes and R. E. P. Winpenny, *Chem. Commun.*, 2011, **47,** 10587;
d) P.-H. Guo, J. Liu, Z.-H. Wu, H. Yan, Y.-C. Chen, J.-H. Jia and M.-L. Tong, *Inorg. Chem.*, 2015, **54,** 8087;
e) T. Pugh, V. Vieru, L. F. Chibotaru and R. A. Layfield, *Chem. Sci.*, 2016, **7,** 2128;
f) T. Pugh, N. F. Chilton and R. A. Layfield, *Chem. Sci.*, 2017, **8,** 2073;
g) J. Xiong, H.-Y. Ding, Y.-S. Meng, C. Gao, X.-J. Zhang, Z.-S. Meng, Y.-Q. Zhang, W. Shi, B.-W. Wang and S. Gao, *Chem. Sci.*, 2017, **8,** 1288;
h) J. D. Rinehart, M. Fang, W. J. Evans and J. R. Long, *J. Am. Chem. Soc*, 2011, **133,** 14236;
i) R. J. Blagg, L. Ungur, F. Tuna, J. Speak, P. Comar, D. Collison, W. Wernsdorfer, E. J. L. McInnes, L. F. Chibotaru and R. E. P. Winpenny, *Nat. Chem.*, 2013, **5,** 673;
j) C. A. Gould, K. R. McClain, D. Reta, J. G. C. Kragskow, D. A. Marchiori, E. Lachman, E.-S. Choi, J. G. Analytis, R. D. Britt, N. F. Chilton, B. G. Harvey and J. R. Long, *Science*, 2022, **375,** 198.

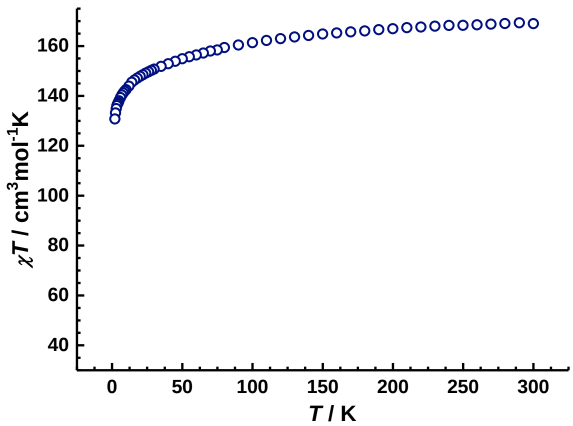

Figure S21. Susceptibility temperature product χT as a function of temperature recorded on **$Dy_{12}(L)_8$** in an applied field of 1 kOe.

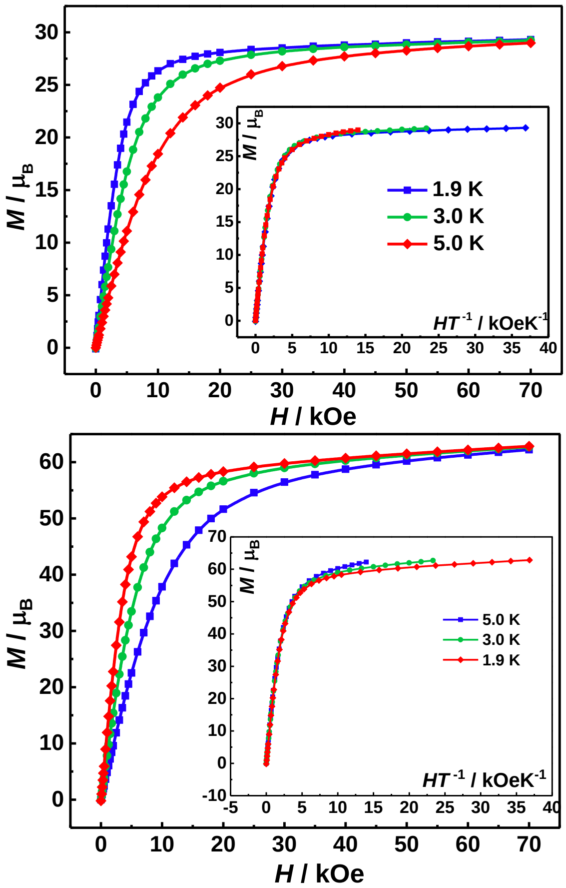

Figure S22. Field dependences of magnetizations in the field range 0–70 kOe and temperature range 1.9–5.0 K for **$Dy_6(L)_6$** (top) and **$Dy_{12}(L)_8$** (bottom). Inset: Plots of the reduced magnetization *M* versus *H*/*T*.

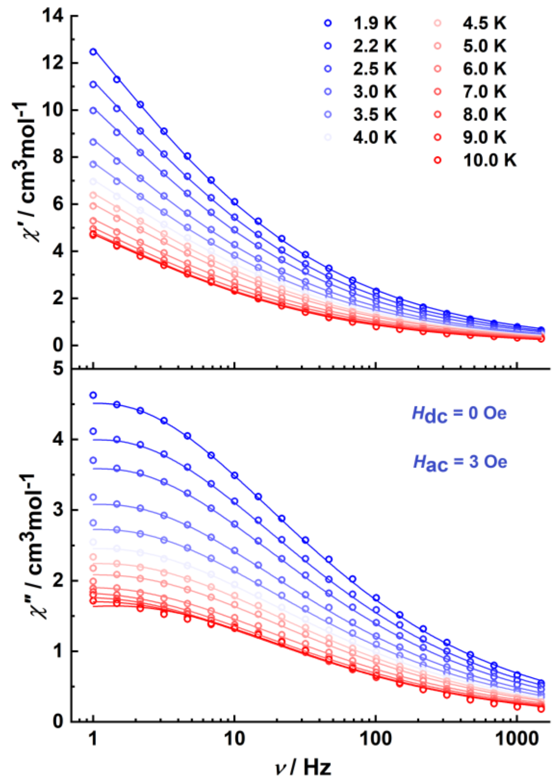

Figure S23. Frequency dependence of the in-phase (χ') and out-of-phase (χ'') ac susceptibility signals for **$Dy_6(L)_6$** between 1.9 and 10 K under zero dc-field. The Solid lines represent the best fit to the generalized Debye model as described in the main text.

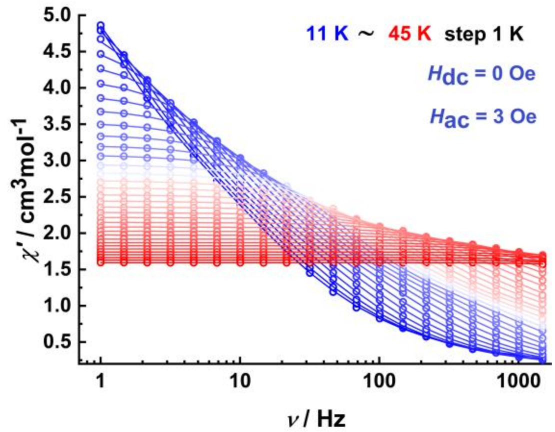

Figure S24. Frequency dependence of the in-phase (χ') ac susceptibility signals for **$Dy_6(L)_6$** between 11 and 45 K under zero dc-field. The solid lines represent fitting of the experimental data at different temperatures using the sum of two modified Debye functions.

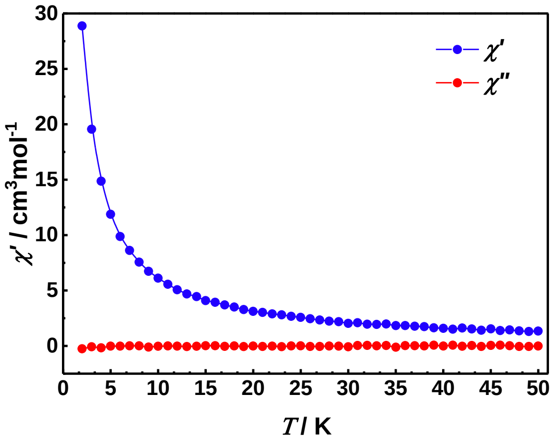

Figure S25. Plots of ac susceptibility *vs*. temperature at H_{ac} = 3.0 Oe, H_{dc} = 0 Oe, oscillating at 1−1488 Hz for **$Dy_{12}(L)_8$** in the temperature range of 2−50 K.

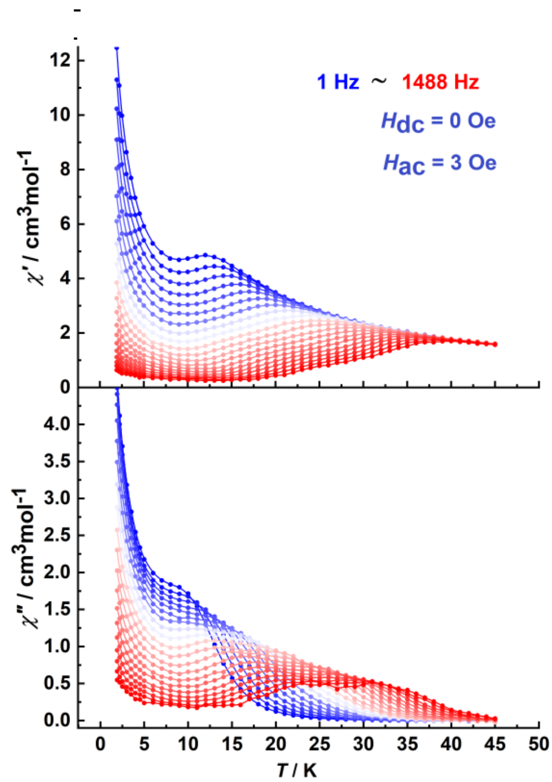

Figure S26. Plots of ac susceptibility *vs*. temperature at H_{ac} = 3.0 Oe, H_{dc} = 0 Oe, oscillating at 1−1488 Hz for **$Dy_6(L)_6$** in the temperature range of 2−45 K.

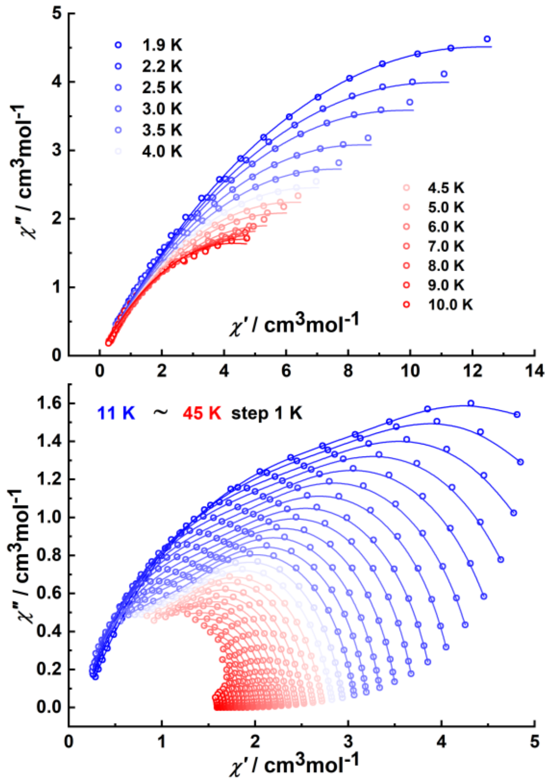

Figure S27. (Top) Cole−Cole plots for temperatures between 1.9 and 10 K under a zero dc field with the best fit to the generalized Debye model for $Dy_6(L)_6$. (bottom) Cole−Cole plots for temperatures between 11 and 45 K under a zero dc field with the best fit to sum of two modified Debye functions with the fitting parameters in Table S8. The Solid lines represent fits to the data, as described inthe main text.

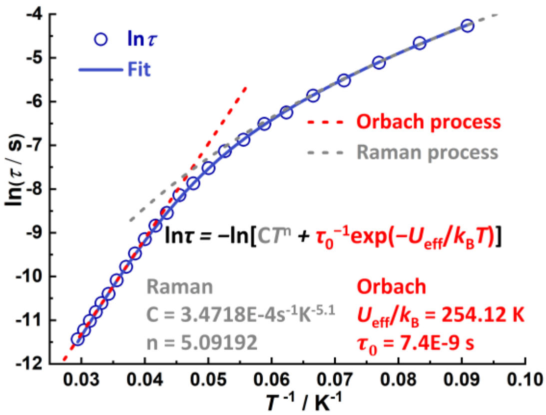

Figure S28. A plot of ln(τ/s) versus T^{-1} for FR of $Dy_6(L)_6$ under zero dc-field, the relaxation times were obtained by simultaneous fitting of Cole–Cole plots (Figure S25). The blue line represents the fit to multiple relaxation processes using Equation 1 (main text). Red and dark blue dashed lines represent individual Orbach and Raman fits, respectively.

Table S7. The best fitting parameters for Cole−Cole plots of **$Dy_6(L)_6$** at varying temperatures under zero applied dc field.

T (K)	χ_T	χ_S	*α*
1.9	24.3234	0.111297E-07	0.5468
2.2	21.5308	0.157138E-07	0.5468
2.5	19.3423	0.230820E-07	0.5470
3.0	16.6821	0.330006E-07	0.5486
3.5	14.8931	0.457238E-07	0.5526
4.0	13.4930	0.640006E-07	0.5551
4.5	12.3720	0.101333E-06	0.5566
5.0	11.6096	0.130973E-06	0.5607
6.0	10.7381	0.157001E-06	0.5663
7.0	10.3377	0.186684E-06	0.5686
8.0	9.77760	0.184327E-06	0.5600
9.0	9.26286	0.288006E-06	0.5508
10.0	8.62511	0.280376E-06	0.5353

Table S8. Relaxation fitting parameters for Cole−Cole plots of **$Dy_6(L)_6$** at varying temperatures under zero applied dc-field using the sum of two modified Debye model.[2]

T (K)	$\chi_{S,\,tol}$	FR $\Delta\chi_1$	τ_1	α_1	SR $\Delta\chi_2$	τ_2	α_2
11	0.1666	4.1648	0.1405E-01	0.3823	2.0043	0.1519	0.0322
12	0.1387	3.8574	0.1041E-01	0.3722	1.8519	0.1049	0.0289
13	0.1431	3.1324	0.6048E-02	0.3346	2.1568	0.07058	0.0862
14	0.1362	2.7307	0.4021E-02	0.3140	2.1849	0.04792	0.1013
15	0.1339	2.3582	0.2604E-02	0.2919	2.2312	0.03314	0.1145
16	0.1404	2.0742	0.1788E-02	0.2774	2.2162	0.02324	0.1231
17	0.0952	2.2338	0.1550E-02	0.3145	1.8369	0.01813	0.0931
18	0.0984	1.9466	0.9961E-03	0.2964	1.8888	0.01303	0.1110
19	0.1118	1.9000	0.7999E-03	0.3083	1.7175	0.01005	0.0983
20	0.0956	1.7197	0.5277E-03	0.3094	1.7237	0.7383E-02	0.1088
21	0.0669	1.6251	0.3557E-03	0.3157	1.6769	0.5588E-02	0.1125
22	0.0909	1.5671	0.2916E-03	0.3185	1.5599	0.4425E-02	0.1101
23	0.267E-05	1.4992	0.1609E-03	0.3492	1.5860	0.3272E-02	0.1276
24	0.409E-05	1.5710	0.1450E-03	0.3788	1.3856	0.2635E-02	0.1086
25	0.628E-05	1.5115	0.1064E-03	0.3826	1.3280	0.2094E-02	0.1158
26	0.749E-05	1.4233	0.7684E-04	0.3901	1.3081	0.1581E-02	0.1337
27	0.698E-05	1.2581	0.4073E-04	0.3907	1.3735	0.1143E-02	0.1505
28	0.104E-04	1.2867	0.3973E-04	0.3679	1.2465	0.9408E-03	0.1505
29	0.229E-04	1.2585	0.2801E-04	0.3477	1.1869	0.7375E-03	0.1489
30	0.429E-04	1.2167	0.2381E-04	0.2879	1.14612	0.5623E-03	0.1599
31	0.689E-04	1.3974	0.2948E-04	0.3083	0.88851	0.4853E-03	0.1420
32	0.127E-03	1.3123	0.1757E-04	0.2767	0.90417	0.3536E-03	0.1515
33	0.434E-03	1.2474	0.1107E-04	0.2150	0.89989	0.2583E-03	0.1423
34	0.826E-03	1.2097	0.1080E-04	0.0127	0.87428	0.2013E-03	0.1523
35	0.114E-02	1.1465	0.5303E-05	0.0203	0.87920	0.1324E-03	0.1600
36	0.355E-02	1.2006	0.5197E-05	0.1385E-07	0.76971	0.9979E-04	0.1569
37	0.0256	1.5143	0.1052E-04	0.1492E-07	0.37689	0.1539E-03	0.0702
38	0.0397	1.3720	0.3211E-05	0.6777E-07	0.45577	0.1007E-03	0.0483
39	0.14169	1.4211	0.5906E-05	0.1275E-12	0.26369	0.1025E-03	0.0568
40	0.04136	1.5718	0.5409E-05	0.3347E-12	0.16834	0.1059E-03	0.0219

$$\chi_{AC}(\omega) = \chi_{S,tot} + \frac{\Delta\chi_1}{1+(i\omega\tau_1)^{(1-\alpha_1)}} + \frac{\Delta\chi_2}{1+(i\omega\tau_2)^{(1-\alpha_2)}} \quad \text{(S1)}$$

References

[1] D. Casanova, M. Llunell, P. Alemany and S. Alvarez, *Chem. Eur. J.*, 2005, **11**, 1479.

[2] Y.-N. Guo, G.-F. Xu, Y. Guo and J. Tang, *Dalton Trans.*, 2011, **40**, 9953.